

# Impact of Atmospheric Circulation on Temperature, Clouds, and Radiation at Summit Station, Greenland, with Self-Organizing Maps

MICHAEL R. GALLAGHER, MATTHEW D. SHUPE, AND NATHANIEL B. MILLER

*Cooperative Institute for Research in Environmental Science, and NOAA/Earth System Research Laboratory, Boulder, Colorado*

(Manuscript received 29 December 2017, in final form 28 August 2018)

## ABSTRACT

The Greenland Ice Sheet (GrIS) plays a crucial role in the Arctic climate, and atmospheric conditions are the primary modifier of mass balance. This analysis establishes the relationship between large-scale atmospheric circulation and principal determinants of GrIS mass balance: moisture, cloud properties, radiative forcing, and temperature. Using self-organizing maps (SOMs), observations from the Integrated Characterization of Energy, Clouds, Atmospheric State, and Precipitation at Summit (ICECAPS) project are categorized by daily sea level pressure (SLP) gradient. The results describe in detail how southerly, northerly, and zonal circulation regimes impact observations at Summit Station, Greenland. This southerly regime is linked to large anomalous increases in low-level liquid cloud formation, cloud radiative forcing (CRF), and surface warming at Summit Station. An individual southerly pattern relates to the largest positive anomalies, with the most extreme 25% of cases leading to CRF anomalies above  $21 \text{ W m}^{-2}$  and temperature anomalies beyond  $8.5^\circ\text{C}$ . Finally, the July 2012 extreme melt event is analyzed, showing that the prolonged ice sheet warming was related to persistence of these southerly circulation patterns, causing an unusually extended period of anomalous CRF and temperature. These results demonstrate a novel methodology, connecting daily atmospheric circulation to a relatively brief record of observations.

## 1. Introduction

Physical changes in the Greenland Ice Sheet (GrIS) have far-reaching implications on regional and global scales. Decreases in GrIS mass balance contribute to rising sea levels and increased freshwater flux, and they modify climate feedback processes (Zwally et al. 2002). If entirely melted, the GrIS contains enough water to raise global sea level by 7.2 m and holds approximately 14% of the world's ice, the most in the Northern Hemisphere (Church et al. 2001). With surface melt of the GrIS increasing in recent time (Mernild et al. 2011), record surface melt occurring in the last decade (Hall et al. 2013), accelerating ice sheet movement as a result of this melt (Zwally et al. 2002; van de Wal et al. 2008), and a rapidly transforming climate (Comiso and Hall 2014), studying Greenland and the surrounding Arctic has never been more important.

At present, the GrIS is not in equilibrium (van de Wal et al. 2008), with global warming increasing ablation in

recent years (Hanna et al. 2008). Since 2009, 84% of the increase in mass loss of the GrIS is from increased surface runoff (Enderlin et al. 2014), with the primary cause of loss being increases in surface air temperatures (Chen et al. 2016). Over the GrIS, these temperatures are strongly impacted by overhead clouds through absorption of outgoing longwave radiation and reflection of incoming shortwave radiation (van den Broeke et al. 2009).

In the Arctic, clouds are the dominant modifier of GrIS surface radiative budget (Shupe and Intrieri 2004) and can increase surface temperatures up to  $9^\circ\text{C}$  from clear-sky conditions (Walsh and Chapman 1998). On the central GrIS, clouds add a net  $33 \text{ W m}^{-2}$  to the annual mean surface energy budget (Miller et al. 2015), and surface temperatures correlate closely with cloud conditions (Miller et al. 2017). The importance of these relationships was made clear by the July 2012 GrIS melt event, where an unprecedented 98.6% of the GrIS experienced surface melt (Nghiem et al. 2012). This extreme event was linked to atmospheric circulation, moisture transport, and the formation of low-level liquid clouds (Neff et al. 2014; Hanna et al. 2014; Bennartz et al. 2013; Solomon et al. 2017). Although clouds and

---

*Corresponding author:* Michael R. Gallagher, michael.ray.gallagher@gmail.com

surface temperatures are closely linked to atmospheric circulation (Chen et al. 2016), the detailed relationships among temperature, radiation, cloud formation, and large-scale atmospheric circulation have yet to be studied over the GrIS. This gap in our understanding is the focus of this paper.

The analysis presented here categorizes GrIS surface observations by atmospheric state, relating daily circulation to variability in processes that impact GrIS mass balance. To construct this relationship, a sufficiently long, continuous, and detailed set of observations must be used. For temperature, moisture, cloud properties, and radiation on the GrIS, these detailed measurements are available only at Summit Station from the Integrated Characterization of Energy, Clouds, Atmospheric State, and Precipitation at Summit (ICECAPS) project. These observations, along with collaborative observations from the National Oceanic and Atmospheric Administration (NOAA) and the Swiss Federal Institute of Technology (ETH) Zürich, provide the principal datasets used here. An overview of these instruments and collection methods can be found in Shupe et al. (2013).

Self-organizing maps (SOMs) and reanalysis data from the National Centers for Environmental Prediction and National Center for Atmospheric Research (NCEP–NCAR) (Kalnay et al. 1996; Kistler et al. 2001) are used to categorize the daily atmospheric circulation affecting the GrIS. Combining the resulting categorization of atmospheric state and the detailed Summit Station surface observations, this analysis creates a complete description of circulation and its effect on temperature, moisture, clouds, and radiative forcing, all of which ultimately impact GrIS energy and mass budgets.

## 2. Data and methods

### a. Circulation classification with SOMs

The SOM algorithm is an unsupervised learning algorithm that creates an objective classification by iteratively grouping similar data vectors (Kohonen 2013; Kohonen et al. 2001). It is capable of reducing large amounts of data to a fundamental map of categories called “nodes.” SOMs, using circulation fields as input, identify a predetermined number of nodes across the data space, such that node distribution represents the data topology and density (Hewitson and Crane 2002). The nonlinear nature of SOMs provides accurate classification of circulation states with very few a priori assumptions.

The result is a robust and generalized map of the primary circulation patterns arranged by similarity that reduces the complex circulation to a subset of categories.

While other methods of classification exist (Huth et al. 2008; Reusch et al. 2005a), SOMs have distinct advantages over alternative techniques and are an established method for categorizing atmospheric circulation (Reusch et al. 2005b, 2007).

The SOM for this analysis (Fig. 1) was created using the SOM PAK, an open-source software toolkit. The SOM PAK has many tuning parameters, with optimizations described in the software manual (Kohonen et al. 1996). When classifying circulation grids, the SOM PAK produces the SOM grid characterizing identified circulation patterns and a list of each day associated with each identified circulation patterns. This list of days then forms the basis for characterizing the impact of each identified atmospheric state.

For the SOM used here, 20 ( $5 \times 4$  dimension) nodes were chosen, balancing the limited availability of Summit Station observations against identifying a broad range of circulation patterns. Relating the Summit Station observational record of approximately 2000 days to the 20-node SOM results in an average sample of 100 days for each circulation pattern, not accounting for missing data. This sample would be reduced to only 57 days per node if using a  $7 \times 5$  SOM. Through empirical testing, it was found that a  $5 \times 4$  SOM resulted in reliable and reproducible results while maintaining the highest dimension classification possible. Detailed descriptions of SOMs and their applications to atmospheric circulation can be found in Crane and Hewitson (2003) and Reusch et al. (2005a).

### b. Reanalysis data

There are many reanalysis products available for research, but each is found to represent atmospheric circulation in the Arctic with similar degrees of accuracy (Lindsay et al. 2014). The NCEP–NCAR reanalysis was chosen here for its overlap with the ICECAPS observation period, as well as the extensive length of available data. NCEP–NCAR circulation fields beginning 1 January 1948 and ending 31 December 2015 were used to identify the primary circulation states of the Greenland domain.

As this research is primarily concerned with daily surface conditions, mean daily SLP from the NCEP–NCAR reanalysis was used. We also tested 850- and 500-hPa height fields, but SLP circulation was more closely related to the surface observations used in this study. Several different spatial domains were tested for their influence on the GrIS. In agreement with prior research (Schuenemann and Cassano 2010; Reusch et al. 2007; Sheridan and Lee 2011), the southern extent of the circulation domain extends south to  $40^\circ\text{N}$ , capturing the connection between midlatitude circulation and conditions over Greenland.

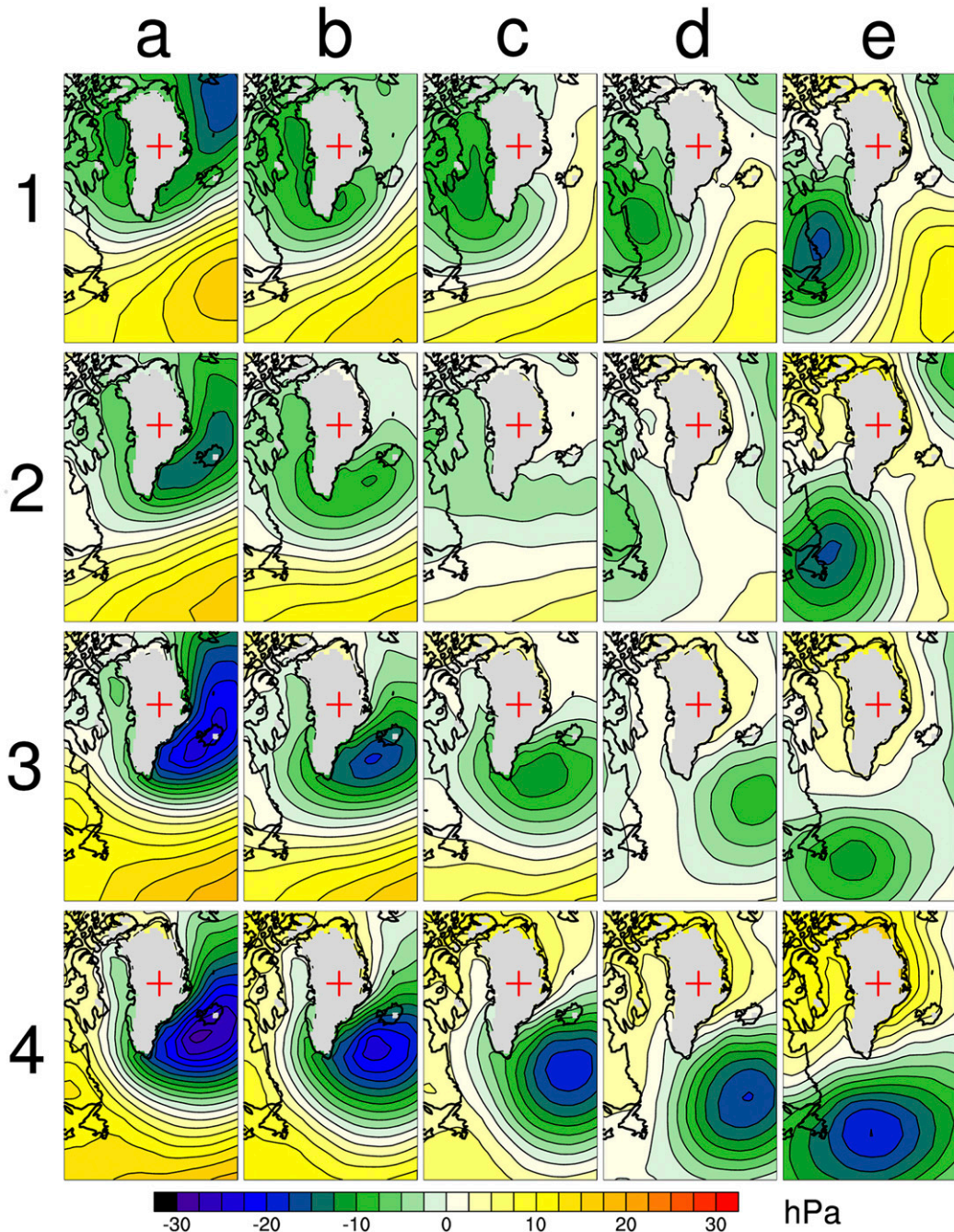


FIG. 1. SOM classification of NCEP-NCAR anomalous SLP fields from 1948 to 2015 (hPa). Plot is of SLP averages from only the years of overlap with Summit Station observations from 2010 to 2015. Anomaly calculated as the difference from the mean daily SLP value across the domain. These data were masked for elevations over 1000 m and are represented in gray. The location of Summit Station is marked by the red cross.

Processing of the circulation data is required before being used in the SOM classification. Grid points above 1000 m (the majority of the Greenland subcontinent) were masked to improve the SOM classification by removing anomalies not related to large-scale regional circulation. The native  $2.5^\circ$  grid spacing of the NCEP-NCAR

data is denser at higher latitudes, and the SLP data were interpolated from the native grid to an equal-area grid with spacing of 50 km. SLP anomalies were calculated by subtracting mean SLP across the domain from the grid of values for each day, producing mean daily SLP gradients. These final SLP gradient fields

capture the circulation features that affect GrIS surface conditions and are used for the construction of the SOM classification.

### c. Surface observations

Although reanalysis data are sufficient for quantifying atmospheric circulation, they do not provide an accurate representation of processes affecting GrIS mass balance, such as moisture, clouds, and radiation (de Boer et al. 2014). In particular, reanalyses poorly quantify the Arctic surface energy budget (Walsh et al. 2009; Zib et al. 2012), with errors greater than  $60 \text{ W m}^{-2}$  in some regions (Serreze et al. 1998; Zib et al. 2012). Instead, detailed and accurate surface measurements are necessary to link regional circulation to processes on the central GrIS.

Observational data used for this analysis are from ICECAPS, an extended field campaign of detailed atmospheric measurements at Summit Station, Greenland ( $72.6^\circ\text{N}$ ,  $38.5^\circ\text{W}$ ; elevation 3255 m). Beginning in May 2010, it was designed to improve understanding of tropospheric properties, surface energy budget, precipitation, and clouds above the central GrIS (Shupe et al. 2013). To support these data, complementary observations of surface broadband radiation and meteorology from NOAA and ETH Zürich were also integrated (Miller et al. 2015). Although measurements at Summit Station lack spatial coverage, these observations are likely representative of the homogeneous central GrIS and are the only observations of these parameters available in this region.

The analysis uses only a subset of these observations, specifically temperature, liquid water path (LWP), precipitable water vapor (PWV), atmospheric profiles of temperature and moisture, and cloud characteristics. Cloud characteristics are determined from ICECAPS data products of cloud composition, cloud occurrence, and cloud radiative forcing (CRF). All available observations from the beginning of measurements in 2010 until the end of 2015 are used here, with intermittent missing data due to the difficulty in making observations at the remote Arctic site. Detailed information on the instrumentation and its measurements can be found in Shupe et al. (2013) and Miller et al. (2015); below are brief descriptions of key products.

Clouds can have large impacts on surface conditions, and CRF is a direct measurement of cloud influence on the GrIS (Miller et al. 2017). CRF measures the instantaneous impact of cloudy conditions on the radiative flux at Earth's surface, relative to the same conditions under an equivalent clear sky. CRF is defined as (Ramanathan et al. 1989; Schneider 1972)

$$\text{CRF} = \text{Flux}_{\text{allsky}} - \text{Flux}_{\text{clearsky}} \quad (1)$$

Here,  $\text{Flux}_{\text{allsky}}$  is the observed net radiative flux at the surface, including the radiative impact of clouds.  $\text{Flux}_{\text{clearsky}}$  is a calculation of the net radiative flux under the same conditions if there had been zero cloud occurrence. At Summit Station, clear-sky calculations are made using the Rapid Radiative Transfer Model (RRTM) with specifications of key atmospheric parameters determined from observations. For more information on the CRF data used here, refer to Miller et al. (2015).

While CRF measures the impact of clouds on surface radiation, observations of the cloud properties affecting CRF are also available at Summit Station. Cloud properties impacting CRF are height, temperature, thickness, and microphysics, as well as surface albedo and solar zenith angle (Shupe and Intrieri 2004). This analysis aims to determine the influence of atmospheric circulation on these cloud characteristics and, thus, the relationships among circulation, clouds, and their radiative impact. Here, cloud composition is defined as the vertical distribution of cloud phase and is derived using phase-specific signatures from radar, lidar, radiosonde, and microwave radiometer measurements, as outlined by Shupe et al. (2006) and Shupe (2007). There are three cloud-phase classification types used in this analysis: 1) mixed phase (any cloud containing liquid water), 2) ice only (clouds that do not contain any liquid), and 3) clear sky (observations without clouds). Though these classifications are a granular tool, they provide the basic information required to understand the relationships among circulation, cloud phase, and surface radiative budget.

Observations at Summit Station are then combined with the SOM using the list of days for each circulation pattern. For plots and figures shown here, averaged values for all days related to a node are calculated. Upper and lower quartiles are also provided to indicate the intranode variability of observation distributions associated with each circulation pattern. The extent to which conclusions can be drawn about specific nodes is limited by this variability, and understanding sources of intranode variability is important for clear interpretation of the results.

Potential sources of intranode variability are as follows:

- Differences in the daily SLP patterns related to each node. SOMs depict the most representative pattern of each node, and thus, not every day related to a node is identical. This could be reduced by the use of a higher-dimensional SOM at the cost of decreased statistics for each node.
- Statistical fluctuations from the brief observational period. Variability could simply represent the small

sample of observations and not the inherent variability of the physical processes. This could be mitigated only by increasing the number of Arctic observations.

- Categorizing of days as discrete data points, neglecting the time evolution of the atmosphere. In reality, daily observations are impacted by the temporal sequence of events. Observations for a pattern can be impacted by the preceding days, and intranode variability can be a result of this hysteresis.
- Observations are only partially constrained by daily SLP used for the SOM. Although tied to upper-level circulation, daily SLP does not capture the complete atmosphere. For this analysis, SLP fields were found to best represent relationships among circulation, cloud processes, and temperature at Summit Station. The 850- and 500-hPa heights had significantly more intranode variability.

As much as possible, the SOM used here was optimized to mitigate factors related to intranode variability. With concern for these caveats, this SOM forms a coherent description of the relationship between atmospheric circulation and processes at Summit Station affecting the GrIS.

#### d. Definition of anomaly

Each SOM circulation pattern occurs uniquely in the annual cycle, and any data evaluated are convoluted with the annual cycle of these data. For example, a predominantly summer node will relate to a higher average temperature than a different node occurring more frequently in winter, regardless of the circulation state. As such, accurately quantifying the annual cycle is necessary to understand the anomalous impact of atmospheric circulation.

Because of the brief observational record, there are distinct challenges in characterizing the annual cycle of parameters in this analysis. With only 5 years of measurements, establishing a climatology for each of these observations is not possible. Instead, an annual cycle of 366 days was constructed by identifying the low-frequency components of each parameter using Fourier decomposition. These annual background series were then subtracted from the daily time series of observations, and the resulting anomaly values were used for the analysis here.

Use of the word “anomaly” in this paper refers to variables calculated using this method. These anomalies represent the difference of a daily parameter from its annual background state. For the remainder of the paper, when a parameter is described as increasing or decreasing, high or low, or positive or negative, it is always in the daily anomaly sense relative to the annual background cycle calculated using the Fourier method.

These words are used to indicate the impact of atmospheric circulation on the daily variability of parameters.

A complete description of the Fourier methodology used here can be found in the [appendix](#).

### 3. Results

Motivated by recent trends in climate ([Richter-Menge et al. 2016](#)) and resulting extreme melt events of the GrIS ([Nghiem et al. 2012](#); [Bennartz et al. 2013](#)), this text focuses primarily on summer warming regimes and their properties, though this analysis does provide a complete circulation description. There is also a primary focus on the occurrence of mixed-phase clouds because of their unique importance to the GrIS ([Miller et al. 2017](#)). In the following sections, there are statements about seasonal relationships between circulation and observed parameters. This discussion was informed by data and plots partitioned by season, though only annual means are shown for the sake of brevity and clarity.

#### a. SOM classification

The SOM classification in this analysis ([Fig. 1](#)) is composed of 20 distinct circulation patterns, with the SOM algorithm placing similar nodes near each other and dissimilar nodes farther apart ([Kohonen 2013](#)). A classification similar to other regional climatological analyses ([Schuenemann and Cassano 2009](#); [Serreze et al. 1997, 1993](#)) is observed here.

Icelandic cyclone systems varying in strength and location can be found in [a, 1], [a, 2], [a, 3], [a, 4], [b, 3], and [b, 4]. Cyclones off the southern tip of the GrIS are described by nodes [c, 3] and [c, 4]. Cyclones located in the North Atlantic are depicted in [d, 3], [d, 4], [e, 3], and [e, 4]. Labrador Sea cyclones to the southwest of the GrIS appear to the upper right in nodes [e, 1], [e, 2], and [d, 1]. Baffin Bay cyclones are located at the top of the SOM in nodes [b, 1] and [c, 1]. Finally, nodes [b, 2], [c, 2], and [d, 2] are patterns with relatively weak circulation. These nodes represent the prominent circulation patterns in the regional circulation, as identified by the SOM algorithm.

Interpretation of the results for these patterns is contingent on understanding their annual distributions. If patterns occurred with equal probability, the expected frequency for each node would be  $100\% / (5 \times 4) = 5\%$ . Instead, the frequency of each node is simply the mean occurrence of this SLP pattern in these reanalysis data. [Figure 2](#) shows the average frequency of occurrence for each node. Node [e, 4] is the most frequent, occurring an average of 7.2% of the year. In contrast, the least frequent node [b, 3] occurs an average of 3.66% of the year.

Monthly distributions of node occurrence are shown in [Fig. 3](#). Most patterns occur in both winter and summer,

	a	b	c	d	e
1	5.61% 123	4.06% 89	5.75% 126	5.98% 131	4.34% 95
2	4.43% 97	5.25% 115	5.02% 110	4.34% 95	5.11% 112
3	6.71% 147	3.29% 72	4.15% 91	5.75% 126	3.51% 77
4	4.61% 101	5.93% 130	5.48% 120	3.79% 83	6.89% 151

FIG. 2. Average node frequency of occurrence for the complete range of NCEP–NCAR data for overlap years from 2010 to 2015. The total number of occurrences for each node from 2010 to 2015 is also given below the frequencies in red. Dark purple colors indicate the most frequent patterns, while dark green colors indicate the most infrequent patterns. White and black text is used only to improve contrast of text for this and other similar plots.

but with significant variation in occurrence probability throughout the year. Many nodes depict cyclones in similar physical locations, differing in strength and seasonal distribution. An example is the Icelandic cyclones occurring primarily in winter, represented by nodes [a, 3], [a, 4], [b, 3], and [b, 4], while weaker Icelandic cyclones occurring primarily in summer are represented by nodes [a, 1] and [a, 2]. Though circulation for these patterns appears visually similar, they are unique in their impact on the GrIS. Annual occurrence distributions indicate that the most frequent regional winter patterns are the strongest Icelandic and North Atlantic cyclones. Conversely, the most frequent summer patterns are strong Baffin Bay cyclones and weaker Icelandic low and North Atlantic cyclones.

Three distinct regimes with significant impact on the central GrIS are identified by this analysis. Northerly

meridional nodes in the left portion of the SOM centered on node [a, 3] describe cyclones to the east of the subcontinent, causing northerly transport across the GrIS along large SLP gradients. Southerly meridional nodes at the top of the SOM centered on node [c, 1] describe cyclones to the west of the subcontinent, causing southerly transport across the GrIS along strong gradients. Zonal nodes are centered on node [d, 4] in the lower-right portion of the SOM, with cyclones to the south of the subcontinent causing zonal transport to the central GrIS.

#### b. Temperature

Node-averaged observations of 2-m temperature anomalies in Fig. 4 show the impact of circulation on temperatures at Summit Station. The three primary

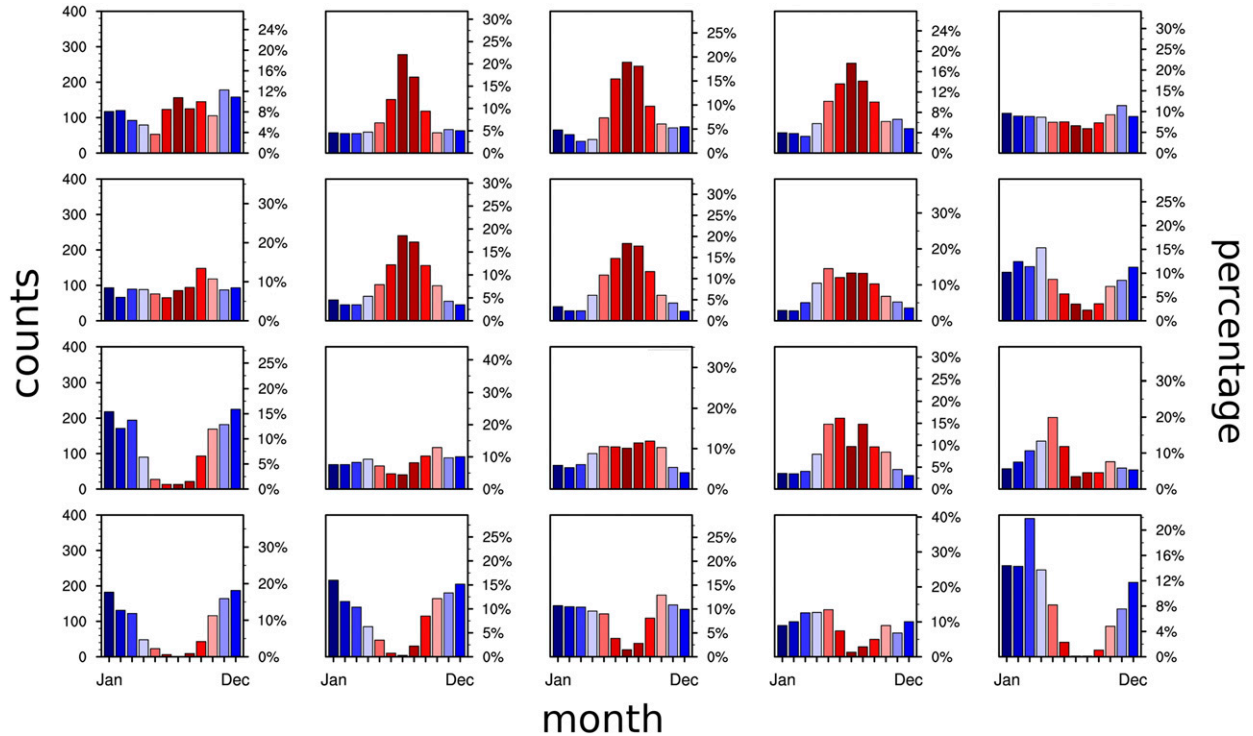


FIG. 3. Histogram quantifying the monthly occurrence of each SOM node for the full NCEP–NCAR reanalysis dataset. Colors indicate the monthly variability of each circulation pattern, with red for summer and blue for winter months.

circulation regimes identified previously have distinct relationships with temperatures at Summit Station.

The largest anomalous temperatures at Summit Station result from southerly circulation, corresponding to Baffin Bay cyclone patterns surrounding SOM node [c, 1]. The magnitude of the anomaly is dependent on the location and strength of the cyclone, with the largest anomalous temperature increase of  $4.58^{\circ}\text{C}$  relating to pattern [c, 1]. For pattern [d, 1], a slight shift of the cyclone core to the south only relates to an average increase of  $2.44^{\circ}\text{C}$ , and a decrease in strength of the pressure gradient relates to a temperature increase of only  $2.71^{\circ}\text{C}$  for node [c, 2]. These southerly circulation patterns are most common in summer, with infrequent occurrences during winter months.

Zonal circulation also relates to anomalous increases in temperature at Summit Station, with lower magnitude than southerly patterns. The largest mean increase in temperature at Summit Station associated with zonal circulation is  $2.13^{\circ}\text{C}$  for node [d, 4]. Zonal patterns surrounding node [d, 4] also relate to moderate anomalous increases in temperature, dependent on the position and strength of the cyclone in the North Atlantic. Each zonal node has a significantly different seasonal distribution, with weaker zonal warming being most frequent in summer (node [d, 3]) and stronger zonal warming being most frequent in winter (node [d, 4]).

While southerly patterns around node [c, 1] occur predominantly in summer, zonal circulation patterns surrounding node [d, 4] occur throughout the year. This variation in seasonal occurrence shows that anomalously warm conditions in summer months are primarily due to frequent strong southerly circulation with small contributions from semifrequent and relatively weak zonal circulation. In winter months, occurrences of southerly patterns are rare, and thus increases in temperature instead relate to strong and semifrequent zonal occurrences.

Intensive cold anomalies occur for the subset of northerly circulation patterns surrounding [a, 3], patterns transporting cold air over the GrIS. All nodes relating to decreases in temperature of more than  $1^{\circ}\text{C}$  are cyclones to the east of the GrIS with northerly transport.

Node-averaged 2-m temperature anomalies from the NCEP–NCAR reanalysis are presented in Fig. 5 for the complete spatial domain. Comparing temperature observations at Summit Station to spatial temperatures from the reanalysis illustrates the importance of the spatial context. Southerly and northerly meridional transport patterns surrounding nodes [c, 1] and [a, 3] show warming and cooling across the extent of the GrIS, coinciding with the largest changes in temperature seen at Summit Station. This indicates that these extreme

	a	b	c	d	e
1	1.69 <b>-2.11</b> -6.26	5.78 <b>1.98</b> -1.86	8.81 <b>4.84</b> 1.24	6.04 <b>2.69</b> -2.19	6.32 <b>0.93</b> -4.74
2	2.17 <b>-2.46</b> -7.22	4.51 <b>0.59</b> -3.14	7.75 <b>2.96</b> -1.78	3.62 <b>0.76</b> -2.87	4.46 <b>-0.16</b> -5.28
3	0.38 <b>-4.34</b> -9.20	1.29 <b>-2.48</b> -6.65	2.71 <b>-0.54</b> -3.86	4.57 <b>1.72</b> -2.22	4.76 <b>0.23</b> -3.28
4	2.04 <b>-2.60</b> -7.68	4.28 <b>-1.53</b> -6.66	7.27 <b>1.09</b> -3.13	6.76 <b>2.38</b> -2.53	6.74 <b>0.78</b> -4.56

FIG. 4. Node-averaged Summit Station 2-m anomalous temperature ( $^{\circ}\text{C}$ ). Positive values (red nodes) indicate anomalous warming on average. Negative values (blue nodes) indicate anomalous cooling on average. Upper and lower quartile bounds are included and represent the distribution of daily average temperature measurements associated with each node.

temperature changes at Summit Station from strong northerly and southerly flow are likely accompanied by temperature changes across the central GrIS. In comparison, zonal patterns surrounding node [d, 4] relate to more moderate and less homogeneous temperature variation at Summit Station and across the GrIS. Notable large temperature gradients are seen in reanalysis data on the central GrIS near Summit Station for nodes [e, 1] and [e, 4], and the impact of these patterns on Summit Station observations is dependent on the position of these gradients. Circulation patterns with large temperature gradients across the central GrIS relate to higher variability in temperature observations. While these data are not sufficient for a detailed study, the spatial patterns give valuable context to the Summit Station temperature observations.

### c. Moisture and clouds

Figure 4 relates circulation patterns to their impact on temperature but does not describe the processes driving these temperature variations. Miller et al. (2017) showed that temperatures in summer months at Summit Station are strongly responsive to CRF from

low-level liquid-bearing clouds. Here, circulation is connected to these mechanisms using PWV, LWP, cloud composition, and water vapor profiles relating atmospheric circulation to cloud processes and their surface impact. Cloud formation over the GrIS relies on the transport of moisture, quantified here by Figs. 6 and 7, showing node-averaged anomalous PWV and LWP observations.

Large positive anomalies in both LWP and PWV at Summit Station are related to southerly patterns surrounding node [c, 1]. Pattern [c, 1] has the largest positive impact on moisture, with a mean LWP increase of  $4.55 \text{ g m}^{-2}$  and 25% of occurrences increasing LWP by more than  $8.04 \text{ g m}^{-2}$ . In tandem, [c, 1] also relates to an average positive PWV anomaly of  $0.69 \text{ mm}$ . These increases are consistent with moist upslope flow caused by cyclones west of the GrIS. Zonal patterns surrounding node [d, 4] relate much less clearly to changes in LWP and PWV, with significantly smaller and more variable anomalies than southerly circulation patterns. In opposition, northerly transport patterns surrounding node [a, 3] are the driest at Summit Station. Upper quartile boundaries for these nodes indicate there is anomalously low

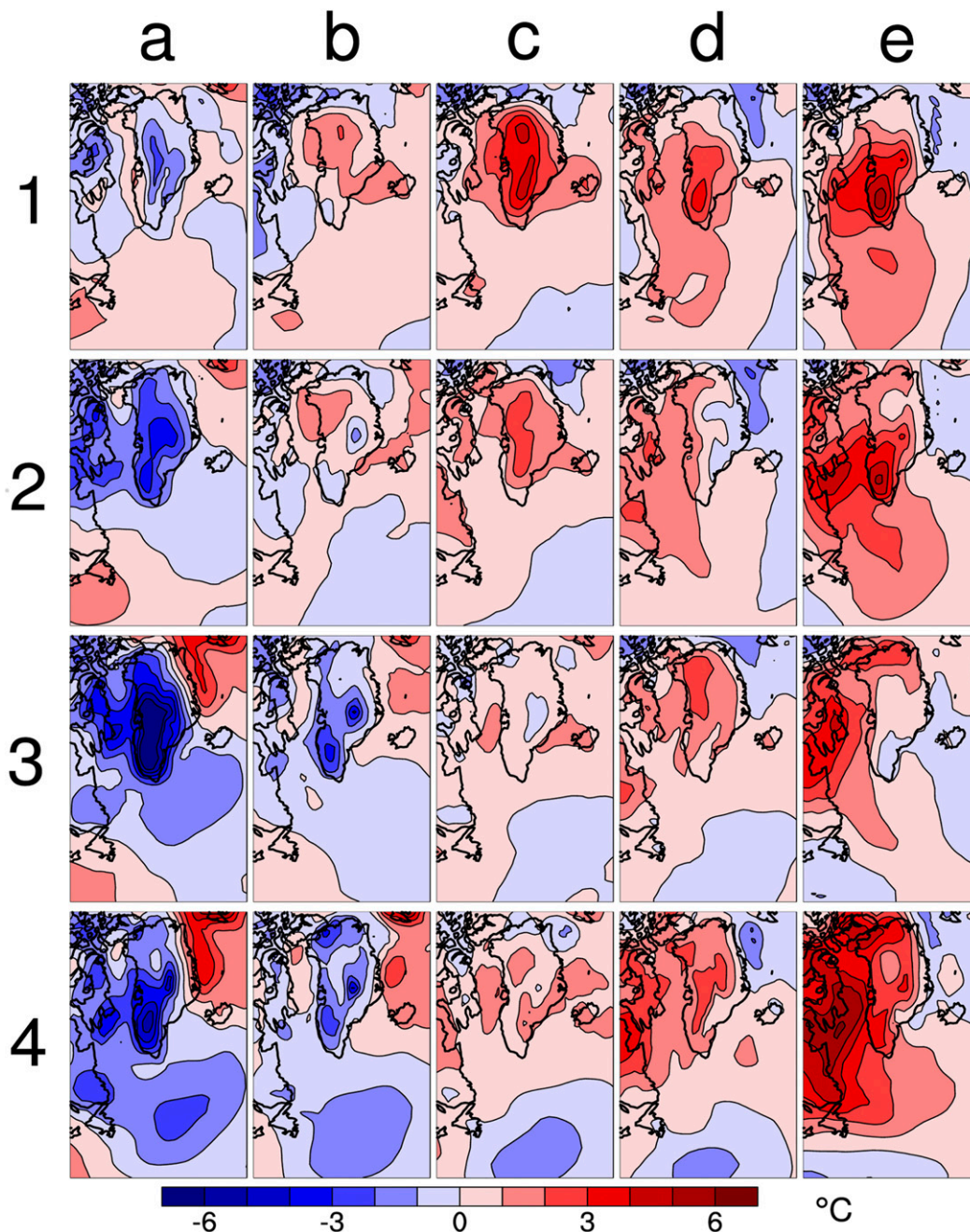


FIG. 5. Node-averaged spatial 2-m temperature anomaly ( $^{\circ}\text{C}$ ) for years 2010–15 from NCEP–NCAR reanalysis data. Anomaly values for reanalysis temperatures were calculated by subtracting the observed value from the average background value for each day of the year (calendar-day mean). Warming trends were removed at each grid point to isolate circulation contribution.

moisture for the majority of occurrences of northerly transport.

The annual cycle of moisture at Summit Station closely follows annual changes in atmospheric circulation. During winter, anomalous increases in moisture result from frequent and strong zonal transport, with moisture increases

only occasionally occurring from very southerly flow events. Conversely, in summer, anomalous increases in moisture are exclusively from frequent strong southerly patterns, with minor contributions from zonal circulation. The shift between these regimes corresponds with the relative differences in the summer and winter mean states.

	a	b	c	d	e
1	-0.08 <b>-0.29</b> -0.58	0.66 <b>0.20</b> -0.43	1.30 <b>0.69</b> -0.06	0.79 <b>0.20</b> -0.54	0.46 <b>-0.02</b> -0.52
2	0.02 <b>-0.28</b> -0.68	0.40 <b>0.05</b> -0.32	1.01 <b>0.38</b> -0.53	0.54 <b>-0.06</b> -0.64	0.22 <b>-0.03</b> -0.46
3	-0.07 <b>-0.34</b> -0.65	0.16 <b>-0.16</b> -0.58	0.35 <b>-0.20</b> -0.63	0.74 <b>0.27</b> -0.54	0.48 <b>0.08</b> -0.46
4	0.01 <b>-0.26</b> -0.46	0.05 <b>-0.19</b> -0.49	0.40 <b>0.01</b> -0.54	0.47 <b>0.14</b> -0.31	0.07 <b>0.01</b> -0.43

FIG. 6. Node-averaged daily PWV anomaly (mm) at Summit Station.

While PWV and LWP provide basic information about moisture, cloud properties affecting surface radiation have a different relationship with atmospheric circulation. Cloud classification using ICECAPS observations is examined from 0- to 5-km altitude over Summit Station. Cloud composition is broken into three simple cloud types: mixed phase (liquid bearing), ice (not liquid bearing), and clear sky. At each height, cloud composition is calculated as the mean percentage of cloud occurrence, such that the sum of all types must equal 100%.

Figure 8 shows the net average fractional occurrence by cloud type as a function of height above Summit Station, and Fig. 9 shows the anomalous values relative to these net occurrences. For mixed-phase cloud occurrence, red shading outlines the quartile bounds of the distribution to indicate variability for each pattern. The quartiles for ice-phase cloud occurrence are not shown for the sake of clarity. Distributions of ice-phase cloud occurrence are broad for all nodes, indicating that ice-phase cloud occurrence is not constrained by SLP circulation to the same degree as mixed-phase occurrence.

Large increases in mixed-phase cloud occurrence relate to southerly transport patterns around node [c, 1],

with anomalous increases at all heights. In particular, nodes [c, 1] and [c, 2] are characterized by the largest increases in mixed-phase cloud occurrence below 1 km at Summit Station, clouds that are critical components of spatially extensive melt (Bennartz et al. 2013). For node [c, 1], anomalous increases in mixed-phase clouds average 8% and net mixed-phase composition of above 20%. This corresponds to approximately 1.7 times the summer average. There is also a corresponding reduction in clear sky, with these southerly patterns having the least clear sky of any circulation patterns. For [c, 1] specifically, clear sky is anomalously reduced more than 15% in the first kilometer, on average.

Zonal patterns around node [d, 4] relate to minor increases in mixed-phase cloud occurrence on average, with limited increases in mixed-phase cloud occurrence in the first 250 m above Summit Station for nodes [d, 4] and [e, 4]. The anomalous impact of zonal circulation on mixed-phase cloud occurrence is significantly less than that of southerly circulation patterns.

Finally, northerly circulation patterns surrounding node [a, 3] relate to decreased mixed-phase cloud occurrence at all heights.

Figure 10 shows node-averaged anomalous water vapor profiles measured by radiosondes at Summit Station.

	a	b	c	d	e
1	-0.83 <b>-3.21</b> -5.57	0.81 <b>-1.05</b> -6.62	8.04 <b>4.55</b> -4.16	6.85 <b>1.71</b> -5.96	4.35 <b>0.32</b> -4.65
2	0.24 <b>-3.07</b> -6.90	1.05 <b>-1.43</b> -7.21	9.96 <b>4.25</b> -6.14	0.89 <b>-2.37</b> -6.71	2.69 <b>0.99</b> -3.30
3	-1.11 <b>-3.55</b> -5.76	0.76 <b>-2.44</b> -5.57	1.91 <b>-1.08</b> -5.94	2.70 <b>-0.27</b> -8.12	3.31 <b>-0.54</b> -4.61
4	-2.08 <b>-3.62</b> -4.91	0.25 <b>-2.49</b> -4.54	2.45 <b>0.60</b> -5.08	4.82 <b>1.33</b> -3.35	1.91 <b>1.48</b> -2.81

FIG. 7. Node-averaged LWP anomaly ( $\text{g m}^{-2}$ ) at Summit Station.

The profiles of water vapor are consistent with integral PWV results and give important additional information about vertical structure. Southerly patterns [b, 1], [d, 1], and [c, 2] relate to average increases in water vapor primarily in the first kilometer, while the strongest southerly node [c, 1] shows increases in water vapor at all heights. Northerly patterns result in a consistent reduction in water vapor at all heights above Summit Station, on average. Consistent changes in vertical structure of water vapor resulting from zonal circulation are limited to relatively small increases in the first 250 m for nodes surrounding [d, 4].

#### d. Cloud radiative forcing

To relate the impact of atmospheric circulation on surface temperatures, cloud impact on radiation must be considered. Miller et al. (2017) have shown that temperature observations at Summit Station are strongly responsive to CRF, particularly from low-level mixed-phase clouds.

The impact of circulation-induced cloud occurrence anomalies on radiation is quantified by node-averaged anomalous CRF in Fig. 11. Large increases in CRF relate to southerly patterns surrounding node [c, 1]. Occurrences of southerly pattern [c, 1] are associated with

an average increase in CRF of  $10.7 \text{ W m}^{-2}$ , the largest of any pattern. In total, 75% of [c, 1] occurrences increase CRF more than  $3.45 \text{ W m}^{-2}$  and 25% of occurrences by more than  $21.1 \text{ W m}^{-2}$ , as shown by node quartiles.

The impact of zonal patterns on CRF is less consistent, with central zonal pattern [d, 4] relating to significant increased CRF, but with decreased CRF values for surrounding patterns [d, 3], [c, 4], and [e, 4]. Occurrences of node [d, 4] increase CRF by an average of  $6.24 \text{ W m}^{-2}$ , while surrounding nodes decrease CRF by an average of  $2.2 \text{ W m}^{-2}$ . While this is large compared to other zonal nodes, the impact is primarily in winter. Northerly patterns surrounding node [a, 3] relate to decreased CRF values at Summit Station, on average.

To distinguish spectral radiative effects, Figs. 12 and 13 decompose CRF into short- and longwave components. The impact of clouds on shortwave CRF is limited to patterns occurring in summer months, with the most significant decreases in shortwave CRF for southerly nodes, due to cloud blocking of shortwave surface transmission. The distinct net CRF impact of zonal node [d, 4] is primarily due to increased longwave CRF. Northerly patterns decrease longwave CRF, while southerly nodes relate to anomalous increases.

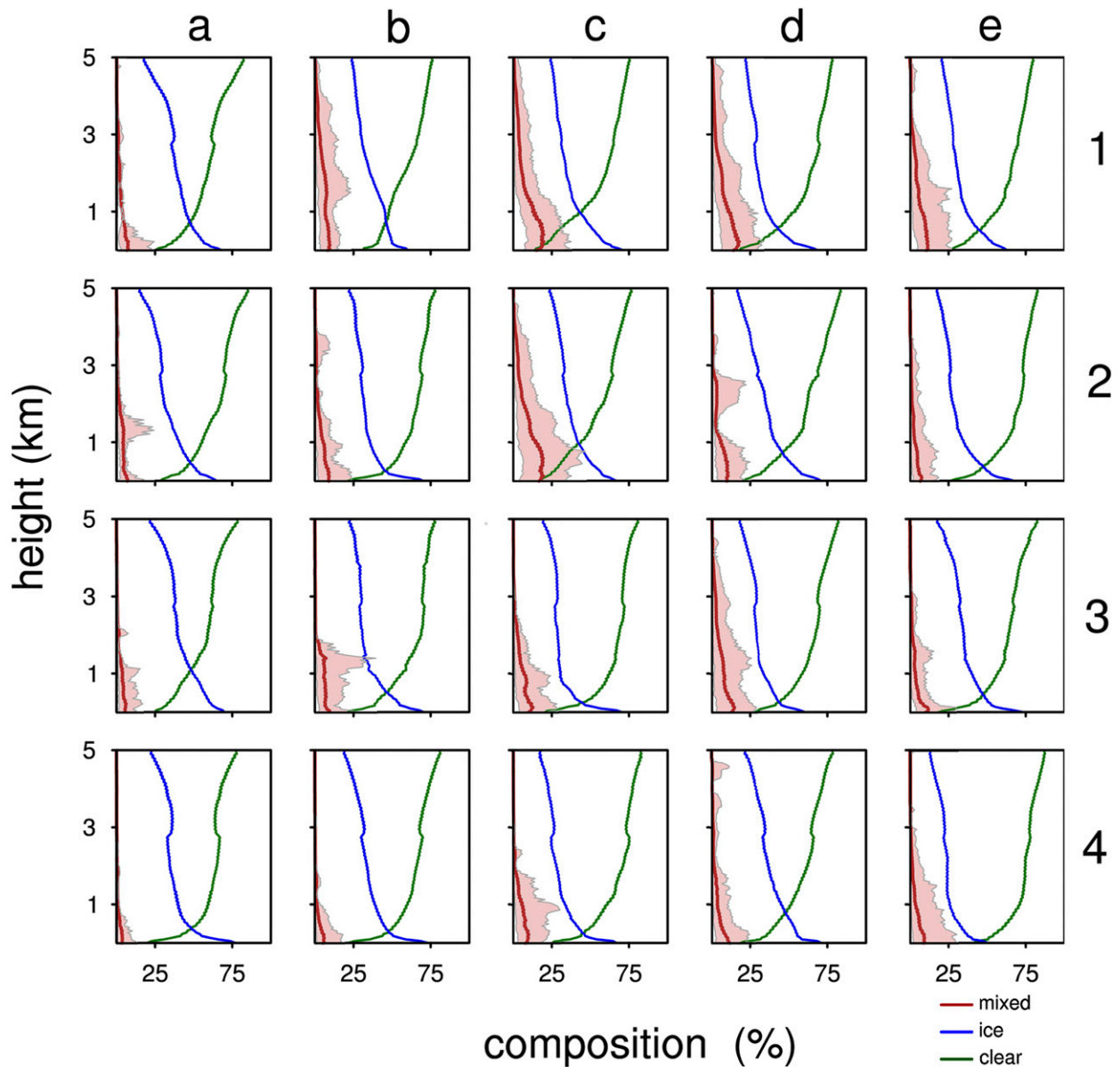


FIG. 8. Node-averaged vertical distribution of cloud composition percentage for each node. Cloud type identified using a multisensor cloud-phase classification algorithm (Shupe 2007). All (100%) cloud occurrence is distributed into three classes: clear sky, ice composition, and mixed-phase composition. Mixed-phase composition clouds are observations of cloud occurrence that have any significant amount of liquid-phase droplets. Red shading indicates the quartile bounds on the distribution for mixed-phase clouds.

#### 4. Discussion

The following section discusses atmospheric circulation and its impact on surface observations, based on measurements at Summit Station from 2010 to 2015. Current research shows that net water vapor transport to Greenland is increasing (Mattingly et al. 2016) and that Arctic dynamics are changing with global warming (Moritz et al. 2002). These larger climate shifts may, in time, modify or amplify the processes studied in this analysis. While the discussion here provides detailed

insight into Arctic processes, continued observations will be necessary to investigate decadal-scale climate variability and the effects of global warming.

##### *a. Circulation, moisture, clouds, and CRF*

In summer months, ablation of the GrIS is enhanced by low-level mixed-phase cloud formation (Bennartz et al. 2013), and this analysis shows that specific classified circulation patterns consistently relate to increased CRF and mixed-phase cloud formation.

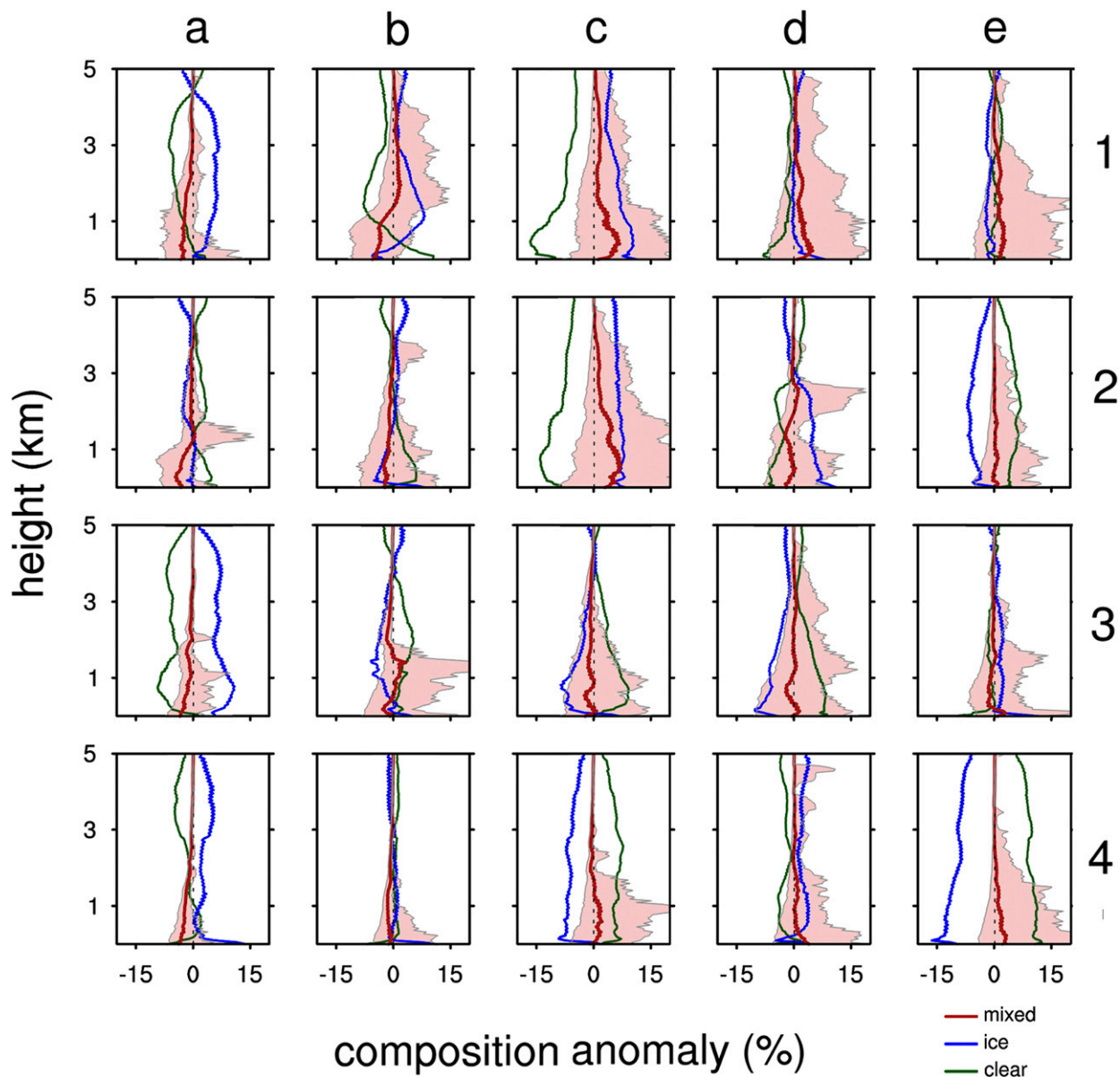


FIG. 9. Node-averaged vertical distribution of anomalous cloud composition anomaly relative to values in Fig. 8. These represent the average change in clouds associated with each node. Upper and lower quartile bounds are given for mixed-phase cloud anomalies to indicate the variability.

The largest daily anomalous increases in moisture and mixed-phase clouds at Summit Station are for circulation patterns with unobstructed southerly onshore flow. For these patterns, the depth and position of the cyclone to the west of the GrIS determine the magnitude of moisture increases, as well as mixed-phase clouds and their corresponding CRF impact. For nodes with large increases in low-level mixed-phase cloud occurrence, there are large increases in longwave radiation at the surface, offset partially by decreased shortwave radiation. This is largest for node [c, 1], where 51 out of the 59

(87%) occurrences of this Baffin Bay cyclone pattern increase CRF. These increases result from increased water vapor, in tandem with large increases in mixed-phase cloud occurrence for the first kilometer above the surface. This circulation pattern is most frequent in summer, with consistent impact on the surface energy budget during months when ablation of the GrIS is most critical.

Zonal circulation patterns are associated with moderate increases in moisture at Summit Station, with nodes [c, 4], [d, 4], [e, 4], and [d, 3] having moderate

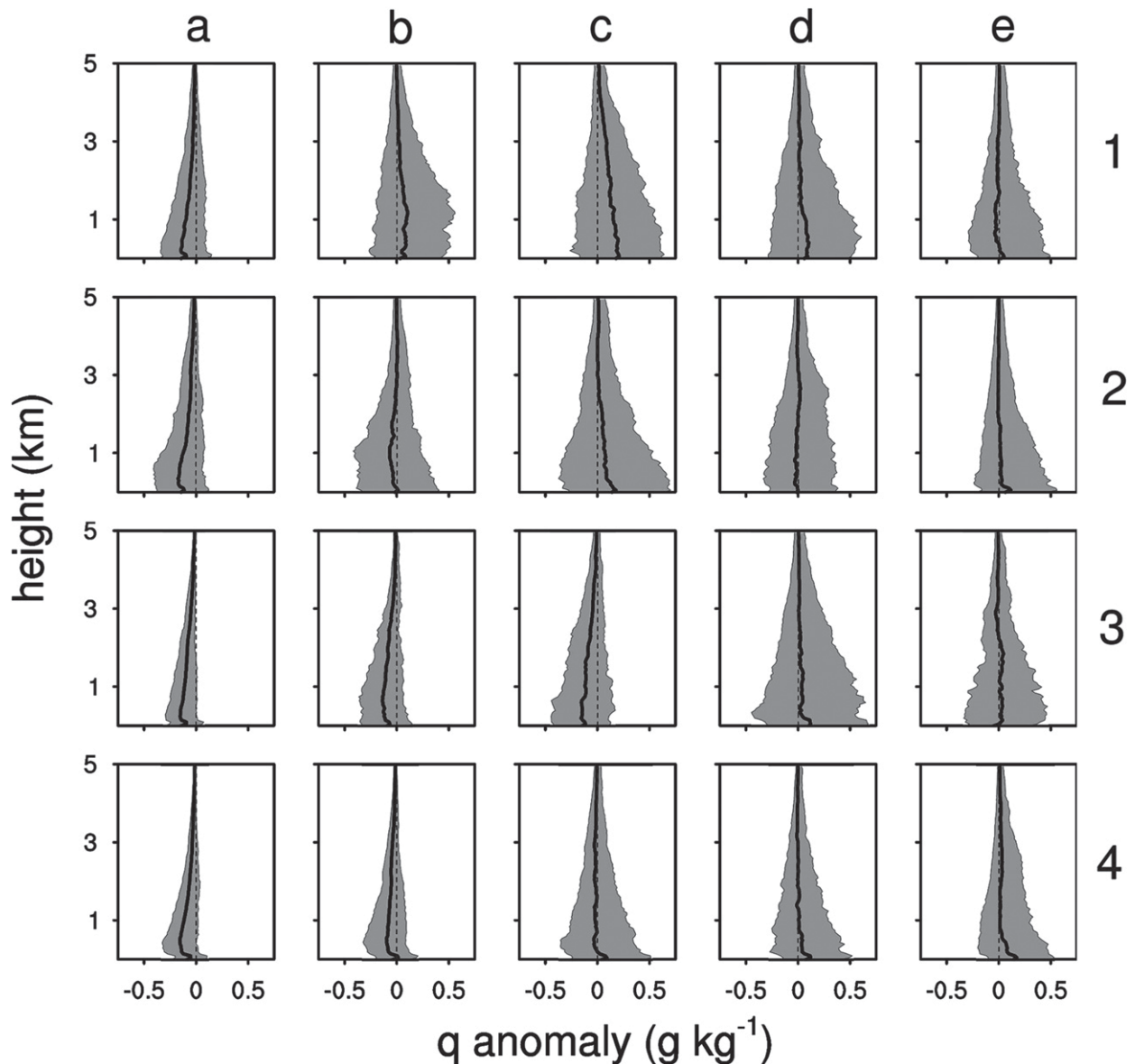


FIG. 10. Node-averaged vertical water vapor anomaly as measured by radiosondes at Summit Station. The solid line is the average water vapor anomaly, while the shaded gray boundary provides the upper and lower quartiles to illustrate variability.

average increases in water vapor at Summit Station in the first 250 m above the surface. For summer zonal pattern [d, 3], there is little anomalous change in mixed-phase cloud occurrence, but a decrease in ice clouds leads to moderate decreases in CRF. For winter zonal patterns, increased low-level mixed-phase cloud occurrence is observed for [c, 4], [d, 4], and [e, 4], but with significant variation in their CRF impact. Node [d, 4] increases CRF by  $6.24 \text{ W m}^{-2}$ , while nodes [c, 4] and [e, 4] decrease CRF by  $-3.5$  and  $-1.5 \text{ W m}^{-2}$ , on average.

The disparity in anomalous CRF impact of zonal patterns is partially explained by the annual occurrence

distribution of these patterns, as there are significant differences in the background state during times when each zonal pattern typically occurs. Summer zonal patterns are dry and low in clouds relative to the summer background state, where winter zonal pattern [d, 4] is relatively moist and cloudy, compared to the winter background state. Rare summer occurrences of [d, 4] were looked at individually and found to have significant anomalous increases in moisture and mixed-phase clouds. This suggests that the circulation associated with [d, 4] is unique in its strength, compared to other zonal patterns.

	a	b	c	d	e
1	6.86 <b>-1.52</b> -13.46	17.21 <b>2.93</b> -10.02	21.10 <b>10.70</b> 3.45	11.90 <b>2.07</b> -13.30	8.07 <b>1.32</b> -9.07
2	10.13 <b>-4.44</b> -17.83	14.00 <b>-2.96</b> -18.09	16.54 <b>3.98</b> -6.05	10.54 <b>0.89</b> -9.56	13.18 <b>-0.43</b> -16.72
3	3.86 <b>-6.10</b> -20.51	13.75 <b>-2.77</b> -15.05	20.28 <b>3.47</b> -14.73	7.67 <b>-3.31</b> -13.77	21.14 <b>2.14</b> -9.89
4	10.25 <b>-2.64</b> -18.03	8.61 <b>-3.18</b> -18.55	8.28 <b>-3.89</b> -17.62	26.69 <b>6.24</b> -8.39	13.24 <b>-0.74</b> -15.51

FIG. 11. Node-averaged net CRF anomaly  $\text{W m}^{-2}$  at Summit Station mapped to the SOM. Positive (red) values indicate nodes with anomalous increases in radiation at the surface of the GrIS, while negative (blue) values indicate patterns with decreasing radiation. Upper and lower quartiles indicate variability.

### b. CRF and temperature

Miller et al. (2017) showed that GrIS surface energy budget, near-surface air temperature, and ground heat flux are modified by clouds and CRF. In this analysis, there are clear relationships between circulation and changes in CRF and temperature. Comparing node-averaged anomalous surface temperature and CRF shows that circulation relating to large changes in CRF also relates to the largest changes in surface temperatures at Summit Station. In particular, southerly and northerly patterns show strong and coherent relationships between temperature and CRF. Southerly pattern [c, 1] relates to the highest CRF and temperature values, with more than 75% of node [c, 1] occurrences increasing both CRF and surface air temperature. Surrounding similar southerly nodes also relate to increases in temperature roughly proportional to their CRF magnitude. In opposition, northerly patterns surrounding [a, 3] with the largest decreases in CRF also relate to the largest decreases in temperature.

For zonal circulation patterns, relationships between changes in CRF and temperature are less clear, with zonal patterns leading to moderate temperature

increases, on average, but only node [d, 4] leading to increased CRF. For [d, 4], large positive CRF is concurrent with average temperature increases. However, surrounding zonal nodes show opposing relationships between CRF and temperature, with mean temperature increases accompanied by moderate decreases in CRF. Thus, for some zonal circulation patterns, clouds are not directly linked to surface air temperature changes.

Although not all changes in CRF occur in parallel with changes in temperature, there is a clear relationship between the largest increases in CRF and the largest anomalous increases in temperatures. Mixed-phase clouds resulting from southerly transport consistently strongly impact both CRF and temperature at the GrIS surface.

### c. July 2012 melt event

While this analysis provides a comprehensive framework to quantify the impact of circulation on the GrIS, prior research has studied the impact of circulation on observations of extreme events. One important case is the July 2012 melt event, where extensive melt of the GrIS reached Summit Station for the first time since

	a	b	c	d	e
1	6.12 <b>-2.59</b> -14.75	20.73 <b>1.49</b> -12.69	27.01 <b>13.16</b> 3.74	22.92 <b>3.63</b> -16.68	14.18 <b>1.80</b> -12.47
2	11.06 <b>-4.86</b> -18.35	15.78 <b>-4.30</b> -20.28	27.05 <b>7.05</b> -4.88	12.07 <b>-0.79</b> -14.51	12.64 <b>-0.58</b> -16.96
3	4.34 <b>-6.10</b> -21.01	8.74 <b>-3.75</b> -17.21	21.49 <b>2.30</b> -15.09	9.98 <b>-5.05</b> -17.68	20.86 <b>1.64</b> -15.98
4	9.90 <b>-2.49</b> -17.04	8.89 <b>-3.26</b> -17.81	8.25 <b>-3.50</b> -18.66	27.22 <b>7.04</b> -8.22	15.26 <b>-1.54</b> -18.12

FIG. 12. As in Fig. 11, but for the longwave component of CRF.

1889 (Nghiem et al. 2012). This melt was primarily a result of broad heating and unique mixed-phase cloud cover from the transport of warm and moist air (Neff et al. 2014; Bennartz et al. 2013; Hanna et al. 2014). The SOM analysis gives a descriptive framework for the days of the melt event, and by examining the 2012 melt event using this framework, methods and conclusions presented here can be contextualized in the larger body of scientific literature.

Table 1 provides information for the days leading up to the 2012 melt event of the node state, net CRF, anomalous CRF, temperature, PWV, and LWP.

For the days leading into the melt event, atmospheric state was categorized by nodes [d, 1] and [e, 1], circulation patterns with moderate southerly transport and strong temperature gradients across the central GrIS. Between 6 and 9 July, this circulation supported modest increases in CRF and temperature at Summit Station resulting from the transport of warm and moist air south of the subcontinent. On 10 July, large increases in PWV, LWP, CRF, and temperature resulted from the previous 4 days of stagnant southerly flow. This consistent southerly transport helped to raise temperatures up to when regional circulation shifted to large anomalies and

southerly transport associated with node [c, 1]. Southerly circulation on 11 July increased LWP by  $45 \text{ g m}^{-2}$ , CRF by  $24 \text{ W m}^{-2}$ , and temperature by  $9.3^\circ\text{C}$ , causing extensive warming across the GrIS, including melt at Summit.

These extreme increases in clouds, CRF, moisture, and temperature are a result of sustained persistent circulation in the southerly transport regime. While this event was extreme in magnitude and duration, analysis results show that occurrences of this southerly circulation consistently relate to anomalous increases in CRF and temperature at Summit Station.

## 5. Conclusions

The GrIS plays a critical role in the global climate, and atmospheric conditions are the primary modifier of GrIS mass balance. The objective of this research was to assess the relationships among atmospheric circulation, clouds, surface energy budget, and temperature variability over the central GrIS. While prior research has quantified how clouds affect surface energy budget, this analysis relates the impact of daily atmospheric circulation to variability in cloud properties, surface radiation, and temperatures.

	a	b	c	d	e
1	1.71 <b>1.33</b> -0.21	3.21 <b>1.37</b> -0.76	1.07 <b>-2.67</b> -7.70	2.21 <b>-1.64</b> -5.88	0.80 <b>-0.69</b> -2.15
2	1.82 <b>0.28</b> -1.58	1.44 <b>1.20</b> -1.46	2.47 <b>-3.21</b> -10.11	6.78 <b>1.71</b> -1.21	1.25 <b>0.17</b> -1.21
3	1.17 <b>0.10</b> -0.38	2.75 <b>1.07</b> -0.29	1.71 <b>0.83</b> -1.09	4.95 <b>1.45</b> -1.07	4.16 <b>0.29</b> -2.35
4	0.77 <b>-0.19</b> -1.10	0.75 <b>0.01</b> -1.20	1.28 <b>-0.35</b> -1.30	1.28 <b>-0.48</b> -1.12	2.21 <b>1.08</b> -0.56

FIG. 13. As in Fig. 11, but for the shortwave component of CRF.

Three primary regimes of circulation driving temperature variability over the central GrIS are identified: southerly meridional, northerly meridional, and zonal. Southerly and northerly meridional transport regimes are directly linked to large anomalous changes in temperature, caused by anomalous changes in mixed-phase cloud occurrence and CRF. For the zonal regime, temperature variability is less reliably linked to mixed-phase cloud formation and CRF.

In the southerly regime, Baffin Bay cyclone node [c, 1] consistently relates to large anomalous increases in radiation and temperature at Summit Station. On 51 of the

59 (87%) days when this pattern occurs, there is an anomalous increase in CRF, with an average increase of  $10.7 \text{ W m}^{-2}$ . In total, 25% of [c, 1] occurrences increase CRF by more than  $21 \text{ W m}^{-2}$ . These large anomalous increases in CRF coincide with an average anomalous increase in temperature of  $4.58^\circ\text{C}$ . During the critical summer months, this southerly regime causes large anomalous increases in mixed-phase cloud formation over the central GrIS, along with corresponding anomalous increases in temperature, moisture, and CRF.

The extreme melt of July 2012 relates to the persistent occurrence of the southerly circulation, causing large

TABLE 1. Key parameters for the Jul 2012 melt event from ICECAPS observations at Summit Station.

Date	Node	Temperature anomaly ( $^\circ\text{C}$ )	Net CRF ( $\text{W m}^{-2}$ )	CRF anomaly ( $\text{W m}^{-2}$ )	PWV anomaly (mm)	LWP anomaly ( $\text{g m}^{-2}$ )
6 Jul	[d, 1]	2.54	39.21	4.09	0.51	4.39
7 Jul	[d, 1]	1.57	41.26	5.77	0.08	-0.29
8 Jul	[e, 1]	-0.86	47.84	12.00	-0.52	4.96
9 Jul	[e, 1]	-3.95	21.8	-14.4	-0.57	-11.4
10 Jul	[e, 1]	6.35	53.67	17.13	3.35	21.93
11 Jul	[c, 1]	9.30	60.86	23.99	1.72	45.02
12 Jul	[b, 1]	8.76	54.54	17.35	2.03	45.40
13 Jul	[b, 2]	6.82	31.68	-5.82	0.50	11.26

increases in clouds, CRF, and temperature. This melt event study demonstrates that the analysis in this paper provides a detailed framework for occurrences of circulation phenomena.

The analysis presented here provides a new methodology, combining established SOM techniques with spectral analysis to quantify the impact of daily circulation on a relatively brief record of cloud properties and atmospheric state. The methodology demonstrates the integral links between regional atmospheric circulation and clouds, radiation, and temperature over the central GrIS. In particular, examining the vertical distribution, phase, LWP, and CRF of clouds as they relate to daily atmospheric circulation makes this analysis unique.

With these methods established, there are several possibilities to extend this research. Summer circulation patterns causing increased CRF and temperatures have an effect on the GrIS surface mass balance, and quantifying this mass loss directly is of great interest. Another possibility is to identify temporal trajectories through SOM space to give insight into events such as the 2012 melt. Methods from this research could also be used to assess models and to test their ability to reproduce circulation-induced related cloud processes. Finally, applying these methods to analyze satellite observations of clouds across the GrIS could give spatial context to the conclusions in this paper.

*Acknowledgments.* This research was supported by the National Science Foundation Grants PLR-1303879 and 1314156 and the NOAA Earth System Research Laboratory. NCEP–NCAR reanalysis data were obtained from the NOAA/ESRL/Physical Science Division in Boulder, Colorado (<http://www.esrl.noaa.gov/psd/>). Thanks to the ICECAPS team, the NOAA/ESRL global monitoring division, the Swiss Federal Research Institute, and the Polar Field Services for maintaining and collecting observations at Summit Station.

## APPENDIX

### Fourier Decomposition of Annual Cycle

Quantifying the annual cycle of observations is a key component to circulation classification with SOMs (Sheridan and Lee 2011). The detailed surface observations from the Arctic used here present unique challenges in this regard, due to the relatively brief observational period. An objective background state is required to isolate the contribution of circulation to the daily variability of observed conditions. While monthly averages provide a useful first glance, they do not capture the gradient between months when large changes in

the atmospheric state can occur in the Arctic for variables of interest. Fourier analysis provides an objective functional description of the background state and models low-frequency changes using observational data.

The annual cycle in observations is derived by first decomposing the original multiyear time series into a group of oscillatory components using the forward Fourier transform algorithm. Then, the highly weighted low-frequency components are selected to capture the annual background state from the observed signal, while excluding the submonthly high-frequency variability of interest to this paper.

For longer time series, this is not necessary, since it is possible to derive the background state using mean values for each day in the annual cycle. For shorter time series, however, daily means are significantly biased by extreme events and other natural variability in observations. Extracting the low-frequency components of the observed time series provides an annual background of daily time steps, excluding these biases to the greatest degree possible. Although other methods to accomplish this exist, the simple near-sinusoidal stationary spectra of these data make the benefits of a more complex analysis moot.

#### a. Fourier decomposition process

This methodology was accomplished in the following steps:

- 1) Detrend and taper data to reduce spectral leakage (Bloomfield 2000).
- 2) Run forward Fourier transform to decompose series into spectral components.
- 3) Reconstruct background state using low-frequency components based on function weight.
- 4) Average components of reconstructed background state to create smooth annual background of 366 days.
- 5) Test resulting background against monthly averages to empirically validate results.

#### b. Results and validation

For this analysis, Fourier components of interest relate to variability occurring for periods of fewer than 15 days. Thus, to construct the annual background state, periods of fewer than 15 days were excluded. The accuracy of the reconstructed annual background was tested by comparing monthly means derived from the reconstructed annual background state to the observed monthly mean values for each parameter (Fig. A1). The result was considered accurate when the reconstructed annual background created using Fourier decomposition reproduced observed monthly means to within 5% accuracy (Fig. A2).

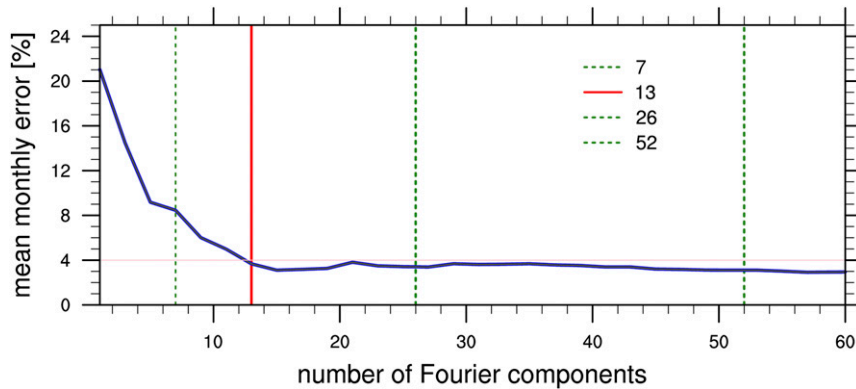


FIG. A1. Percent accuracy of the monthly mean CRF values from Fourier decomposition measured against mean monthly CRF observations. Accuracy is quantified as the absolute value of the difference between each Fourier series monthly mean and the observed monthly means, expressed in percentage and plotted against the number of Fourier components for each series.

Figure A1 shows the mean error in monthly mean reconstruction as a function of the number of low-frequency Fourier components for CRF observations at Summit Station. This was determined by first calculating monthly means for these different Fourier series components and then subtracting this value from monthly mean of observations. The results are represented as a percentage of the average observed CRF for all time, showing that the first-order (single lowest frequency) Fourier series reconstructs mean monthly observations with an error of 22%, on average, while the seventh-order reconstruction (seven lowest frequencies) has errors of 9%, on average. The mean error reaches an asymptotic value at just under 4%. Thus, the minimum number of components required to accurately reproduce monthly means from the annual background is 13 for CRF.

Figure A2 depicts the annual background state produced from the range of possible Fourier components

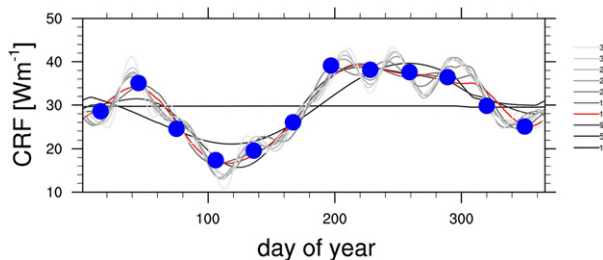


FIG. A2. Testing the representation of the annual CRF cycle throughout the year. Blue points are the monthly mean values of observations, and underlying lines are background series resulting from the Fourier decomposition of daily CRF for a varying number of low-frequency components. Numbers for each line are the total number of components contained in the composite function. The lowest number (i.e., 1) is only the mean observed value. The highest number (i.e., 37) contains the 37 lowest-frequency components of the Fourier decomposition.

and shows that reconstructed series comprised of more than 13 components (periods of fewer than 2 weeks) “overfit” the monthly mean values.

An example of a reconstructed annual background used for this analysis is given in Fig. A3, showing the low-frequency variability in mixed-phase cloud occurrence at Summit Station as a function of height. For profile observations such as this, Fourier decomposition is employed independently at each height.

The sensitivity of the analysis results to attributes of the Fourier-derived background state were tested, and conclusions did not significantly change in magnitude for backgrounds using a reasonable number of Fourier

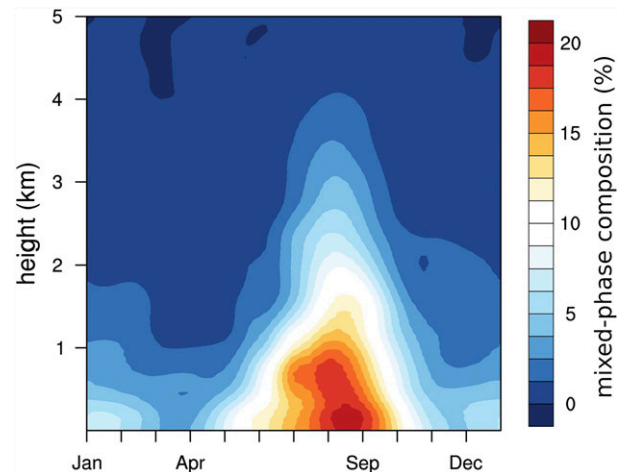


FIG. A3. Annual background state of mixed-phase cloud occurrence as a function of height at Summit Station, identified by Fourier decomposition. These are the values used to calculate daily anomalous cloud composition as a function of height. Near the surface, background mixed-phase cloud occurrence at Summit Station is approximately 15% for all observations in the month of August.

components. For example, although the optimal number of components for CRF was identified to be 13, node-averaged anomaly results did not change significantly for 10–16 components. This lack of sensitivity indicates that observations used here are most impacted by high-frequency variability related to atmospheric circulation and that the results and conclusions are robust beyond subtle choices in the methodology.

## REFERENCES

- Bennartz, R., and Coauthors, 2013: July 2012 Greenland melt extent enhanced by low-level liquid clouds. *Nature*, **496**, 83–86, <https://doi.org/10.1038/nature12002>.
- Bloomfield, P., 2000: *Fourier Analysis of Time Series: An Introduction*. Wiley and Sons, 261 pp.
- Chen, L., X. Fettweis, E. M. Knudsen, and O. M. Johannessen, 2016: Impact of cyclonic and anticyclonic activity on Greenland Ice Sheet surface mass balance variation during 1980–2013. *Int. J. Climatol.*, **36**, 3423–3433, <https://doi.org/10.1002/joc.4565>.
- Church, J., and Coauthors, 2001: Changes in sea level. *Climate Change 2001: The Scientific Basis*, J. T. Houghton et al., Eds., Cambridge University Press, 639–693, <https://www.ipcc.ch/ipccreports/tar/wg1/pdf/TAR-11.PDF>.
- Comiso, J. C., and D. K. Hall, 2014: Climate trends in the Arctic as observed from space. *Wiley Interdiscip. Rev.: Climate Change*, **5**, 389–409, <https://doi.org/10.1002/wcc.277>.
- Crane, R., and B. Hewitson, 2003: Clustering and upscaling of station precipitation records to regional patterns using self-organizing maps (SOMs). *Climate Res.*, **25**, 95–107, <https://doi.org/10.3354/cr025095>.
- de Boer, G., and Coauthors, 2014: Near-surface meteorology during the Arctic Summer Cloud Ocean Study (ASCOS): Evaluation of reanalyses and global climate models. *Atmos. Chem. Phys.*, **14**, 427–445, <https://doi.org/10.5194/acp-14-427-2014>.
- Enderlin, E. M., I. M. Howat, S. Jeong, M. J. Noh, J. H. van Angelen, and M. R. van den Broeke, 2014: An improved mass budget for the Greenland Ice Sheet. *Geophys. Res. Lett.*, **41**, 866–872, <https://doi.org/10.1002/2013GL059010>.
- Hall, D. K., J. C. Comiso, N. E. DiGirolamo, C. A. Shuman, J. E. Box, and L. S. Koenig, 2013: Variability in the surface temperature and melt extent of the Greenland Ice Sheet from MODIS. *Geophys. Res. Lett.*, **40**, 2114–2120, <https://doi.org/10.1002/grl.50240>.
- Hanna, E., and Coauthors, 2008: Increased runoff from melt from the Greenland Ice Sheet: A response to global warming. *J. Climate*, **21**, 331–341, <https://doi.org/10.1175/2007JCLI1964.1>.
- , and Coauthors, 2014: Atmospheric and oceanic climate forcing of the exceptional Greenland Ice Sheet surface melt in summer 2012. *Int. J. Climatol.*, **34**, 1022–1037, <https://doi.org/10.1002/joc.3743>.
- Hewitson, B. C., and R. G. Crane, 2002: Self-organizing maps: Applications to synoptic climatology. *Climate Res.*, **22**, 13–26, <https://doi.org/10.3354/cr022013>.
- Huth, R., C. Beck, A. Philipp, M. Demuzere, Z. Ustrnul, M. Cahynová, J. Kyselý, and O. E. Tveito, 2008: Classifications of atmospheric circulation patterns. *Ann. N.Y. Acad. Sci.*, **1146**, 105–152, <https://doi.org/10.1196/annals.1446.019>.
- Kalnay, E., and Coauthors, 1996: The NCEP/NCAR 40-Year Reanalysis Project. *Bull. Amer. Meteor. Soc.*, **77**, 437–472, [https://doi.org/10.1175/1520-0477\(1996\)077<0437:TNYRP>2.0.CO;2](https://doi.org/10.1175/1520-0477(1996)077<0437:TNYRP>2.0.CO;2).
- Kistler, R., and Coauthors, 2001: The NCEP–NCAR 50-Year Reanalysis: Monthly means CD-ROM and documentation. *Bull. Amer. Meteor. Soc.*, **82**, 247–267, [https://doi.org/10.1175/1520-0477\(2001\)082<0247:TNNYRM>2.3.CO;2](https://doi.org/10.1175/1520-0477(2001)082<0247:TNNYRM>2.3.CO;2).
- Kohonen, T., 2013: Essentials of the self-organizing map. *Neural Networks*, **37**, 52–65, <https://doi.org/10.1016/j.neunet.2012.09.018>.
- , J. Hynninen, J. Kangas, and J. Laaksonen, 1996: SOM\_PAK: The Self-Organizing Map Program Package. Helsinki University of Technology Rep. A31, 27 pp.
- , M. R. Schroeder, and T. S. Huang, Eds., 2001: *Self-Organizing Maps*. 3rd ed. Springer, 501 pp.
- Lindsay, R., M. Wensnahan, A. Schweiger, and J. Zhang, 2014: Evaluation of seven different atmospheric reanalysis products in the Arctic. *J. Climate*, **27**, 2588–2606, <https://doi.org/10.1175/JCLI-D-13-00014.1>.
- Mattingly, K. S., C. A. Ramseyer, J. J. Rosen, T. L. Mote, and R. Muthyala, 2016: Increasing water vapor transport to the Greenland Ice Sheet revealed using self-organizing maps. *Geophys. Res. Lett.*, **43**, 9250–9258, <https://doi.org/10.1002/2016GL070424>.
- Mernild, S. H., T. L. Mote, and G. E. Liston, 2011: Greenland Ice Sheet surface melt extent and trends: 1960–2010. *J. Glaciol.*, **57**, 621–628, <https://doi.org/10.3189/002214311797409712>.
- Miller, N. B., M. D. Shupe, C. J. Cox, V. P. Walden, D. D. Turner, and K. Steffen, 2015: Cloud radiative forcing at Summit, Greenland. *J. Climate*, **28**, 6267–6280, <https://doi.org/10.1175/JCLI-D-15-0076.1>.
- , —, —, D. Noone, P. O. G. Persson, and K. Steffen, 2017: Surface energy budget responses to radiative forcing at Summit, Greenland. *Cryosphere*, **11**, 497–516, <https://doi.org/10.5194/tc-11-497-2017>.
- Moritz, R. E., C. M. Bitz, and E. J. Steig, 2002: Dynamics of recent climate change in the Arctic. *Science*, **297**, 1497–1502, <https://doi.org/10.1126/science.1076522>.
- Neff, W., G. P. Compo, F. Martin Ralph, and M. D. Shupe, 2014: Continental heat anomalies and the extreme melting of the Greenland ice surface in 2012 and 1889. *J. Geophys. Res. Atmos.*, **119**, 6520–6536, <https://doi.org/10.1002/2014JD021470>.
- Nghiem, S. V., and Coauthors, 2012: The extreme melt across the Greenland Ice Sheet in 2012. *Geophys. Res. Lett.*, **39**, L20502, <https://doi.org/10.1029/2012GL053611>.
- Ramanathan, V., R. D. Cess, E. F. Harrison, P. Minnis, B. R. Barkstrom, E. Ahmad, and D. Hartmann, 1989: Cloud-radiative forcing and climate: Results from the Earth Radiation Budget Experiment. *Science*, **243**, 57–63, <https://doi.org/10.1126/science.243.4887.57>.
- Reusch, D. B., R. B. Alley, and B. C. Hewitson, 2005a: Relative performance of self-organizing maps and principal component analysis in pattern extraction from synthetic climatological data. *Polar Geogr.*, **29**, 188–212, <https://doi.org/10.1080/789610199>.
- , B. C. Hewitson, and R. B. Alley, 2005b: Towards ice-core-based synoptic reconstructions of west Antarctic climate with artificial neural networks. *Int. J. Climatol.*, **25**, 581–610, <https://doi.org/10.1002/joc.1143>.
- , R. B. Alley, and B. C. Hewitson, 2007: North Atlantic climate variability from a self-organizing map perspective. *J. Geophys. Res.*, **112**, D02104, <https://doi.org/10.1029/2006JD007460>.
- Richter-Menge, J., J. E. Overland, and J. T. Mathis, 2016: Arctic Report Card 2016: Persistent warming trend and loss of sea ice

- are triggering extensive Arctic changes. NOAA, <http://www.arctic.noaa.gov/Report-Card>.
- Schneider, S., 1972: Cloudiness as a global climatic feedback mechanism: The effects on the radiation balance and surface temperature of variations in cloudiness. *J. Atmos. Sci.*, **29**, 1413–1422, [https://doi.org/10.1175/1520-0469\(1972\)029<1413:CAAGCF>2.0.CO;2](https://doi.org/10.1175/1520-0469(1972)029<1413:CAAGCF>2.0.CO;2).
- Schuenemann, K. C., and J. J. Cassano, 2009: Changes in synoptic weather patterns and Greenland precipitation in the 20th and 21st centuries: 1. Evaluation of late 20th century simulations from IPCC models. *J. Geophys. Res.*, **114**, D20113, <https://doi.org/10.1029/2009JD011705>.
- , and —, 2010: Changes in synoptic weather patterns and Greenland precipitation in the 20th and 21st centuries: 2. Analysis of 21st century atmospheric changes using self-organizing maps. *J. Geophys. Res.*, **115**, D05108, <https://doi.org/10.1029/2009JD011706>.
- Serreze, M. C., J. E. Box, R. G. Barry, and J. E. Walsh, 1993: Characteristics of Arctic synoptic activity, 1952–1989. *Meteor. Atmos. Phys.*, **51**, 147–164, <https://doi.org/10.1007/BF01030491>.
- , F. Carse, R. G. Barry, and J. C. Rogers, 1997: Icelandic low cyclone activity: Climatological features, linkages with the NAO, and relationships with recent changes in the Northern Hemisphere circulation. *J. Climate*, **10**, 453–464, [https://doi.org/10.1175/1520-0442\(1997\)010<0453:ILCACF>2.0.CO;2](https://doi.org/10.1175/1520-0442(1997)010<0453:ILCACF>2.0.CO;2).
- , J. R. Key, J. E. Box, J. A. Maslanik, and K. Steffen, 1998: A new monthly climatology of global radiation for the Arctic and comparisons with NCEP–NCAR reanalysis and ISCCP–C2 fields. *J. Climate*, **11**, 121–136, [https://doi.org/10.1175/1520-0442\(1998\)011<0121:ANMCOG>2.0.CO;2](https://doi.org/10.1175/1520-0442(1998)011<0121:ANMCOG>2.0.CO;2).
- Sheridan, S. C., and C. C. Lee, 2011: The self-organizing map in synoptic climatological research. *Prog. Phys. Geogr.*, **35**, 109–119, <https://doi.org/10.1177/0309133310397582>.
- Shupe, M. D., 2007: A ground-based multisensor cloud phase classifier. *Geophys. Res. Lett.*, **34**, L22809, <https://doi.org/10.1029/2007GL031008>.
- , and J. M. Intrieri, 2004: Cloud radiative forcing of the Arctic surface: The influence of cloud properties, surface albedo, and solar zenith angle. *J. Climate*, **17**, 616–628, [https://doi.org/10.1175/1520-0442\(2004\)017<0616:CRFOTA>2.0.CO;2](https://doi.org/10.1175/1520-0442(2004)017<0616:CRFOTA>2.0.CO;2).
- , S. Y. Matrosov, and T. Uttal, 2006: Arctic mixed-phase cloud properties derived from surface-based sensors at SHEBA. *J. Atmos. Sci.*, **63**, 697–711, <https://doi.org/10.1175/JAS3659.1>.
- , and Coauthors, 2013: High and dry: New observations of tropospheric and cloud properties above the Greenland Ice Sheet. *Bull. Amer. Meteor. Soc.*, **94**, 169–186, <https://doi.org/10.1175/BAMS-D-11-00249.1>.
- Solomon, A., M. D. Shupe, and N. B. Miller, 2017: Cloud–atmospheric boundary layer–surface interactions on the Greenland Ice Sheet during the July 2012 extreme melt event. *J. Climate*, **30**, 3237–3252, <https://doi.org/10.1175/JCLI-D-16-0071.1>.
- van den Broeke, M., P. Smeets, and J. Ettema, 2009: Surface layer climate and turbulent exchange in the ablation zone of the west Greenland Ice Sheet. *Int. J. Climatol.*, **29**, 2309–2323, <https://doi.org/10.1002/joc.1815>.
- van de Wal, R. S. W., W. Boot, M. R. van den Broeke, C. J. P. P. Smeets, C. H. Reijmer, J. J. A. Donker, and J. Oerlemans, 2008: Large and rapid melt-induced velocity changes in the ablation zone of the Greenland Ice Sheet. *Science*, **321**, 111–113, <https://doi.org/10.1126/science.1158540>.
- Walsh, J. E., and W. L. Chapman, 1998: Arctic cloud–radiation–temperature associations in observational data and atmospheric reanalyses. *J. Climate*, **11**, 3030–3045, [https://doi.org/10.1175/1520-0442\(1998\)011<3030:ACRTAI>2.0.CO;2](https://doi.org/10.1175/1520-0442(1998)011<3030:ACRTAI>2.0.CO;2).
- , —, and D. H. Portis, 2009: Arctic cloud fraction and radiative fluxes in atmospheric reanalyses. *J. Climate*, **22**, 2316–2334, <https://doi.org/10.1175/2008JCLI2213.1>.
- Zib, B. J., X. Dong, B. Xi, and A. Kennedy, 2012: Evaluation and intercomparison of cloud fraction and radiative fluxes in recent reanalyses over the Arctic using BSRN surface observations. *J. Climate*, **25**, 2291–2305, <https://doi.org/10.1175/JCLI-D-11-00147.1>.
- Zwally, H., W. Abdalati, T. Herring, K. Larson, J. Saba, and K. Steffen, 2002: Surface melt-induced acceleration of Greenland Ice-Sheet flow. *Science*, **297**, 218–222, <https://doi.org/10.1126/science.1072708>.